NASA/TM–20210014683

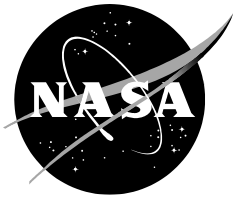

Experimental Flight Validation of the Prandtl 1933 Bell Spanload

Albion H. Bowers, Oscar J. Murillo, David E. Berger, Victoria S. Hawkins, Loren J. Newton, Abbigail G. Waddell, Emily D. Glover, Jesse C. Brady, and John K. Bodylski
Armstrong Flight Research Center, Edwards, California, 93523

Robert "Red" Jensen, and Rebecca A. Bowers (nee Richardson)
Jacobs Technology, Inc., Edwards, California 93523

Christian Gelzer
Logical Innovations, Inc., Edwards, California 93523

Deborah R. Jackson, and Rachel J. Suitor
Universities Space Research Association, Edwards, California 93523

July 2021

NASA STI Program Report Series

The NASA STI Program collects, organizes, provides for archiving, and disseminates NASA's STI. The NASA STI program provides access to the NTRS Registered and its public interface, the NASA Technical Reports Server, thus providing one of the largest collections of aeronautical and space science STI in the world. Results are published in both non-NASA channels and by NASA in the NASA STI Report Series, which includes the following report types:

- TECHNICAL PUBLICATION. Reports of completed research or a major significant phase of research that present the results of NASA Programs and include extensive data or theoretical analysis. Includes compilations of significant scientific and technical data and information deemed to be of continuing reference value. NASA counter-part of peer-reviewed formal professional papers but has less stringent limitations on manuscript length and extent of graphic presentations.

- TECHNICAL MEMORANDUM. Scientific and technical findings that are preliminary or of specialized interest, e.g., quick release reports, working papers, and bibliographies that contain minimal annotation. Does not contain extensive analysis.

- CONTRACTOR REPORT. Scientific and technical findings by NASA-sponsored contractors and grantees.

- CONFERENCE PUBLICATION. Collected papers from scientific and technical conferences, symposia, seminars, or other meetings sponsored or co-sponsored by NASA.

- SPECIAL PUBLICATION. Scientific, technical, or historical information from NASA programs, projects, and missions, often concerned with subjects having substantial public interest.

- TECHNICAL TRANSLATION. English-language translations of foreign scientific and technical material pertinent to NASA's mission.

Specialized services also include organizing and publishing research results, distributing specialized research announcements and feeds, providing information desk and personal search support, and enabling data exchange services.

For more information about the NASA STI program, see the following:

- Access the NASA STI program home page at http://www.sti.nasa.gov

- Help desk contact information:

https://www.sti.nasa.gov/sti-contact-form/
and select the "General" help request type.

NASA/TM–20210014683

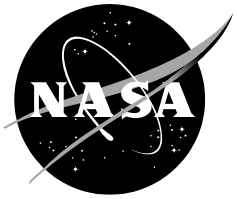

Experimental Flight Validation of the Prandtl 1933 Bell Spanload

Albion H. Bowers, Oscar J. Murillo, David E. Berger, Victoria S. Hawkins, Loren J. Newton, Abbigail G. Waddell, Emily D. Glover, Jesse C. Brady, and John K. Bodylski
Armstrong Flight Research Center, Edwards, California, 93523

Robert "Red" Jensen, and Rebecca A. Bowers (nee Richardson)
Jacobs Technology, Inc., Edwards, California 93523

Christian Gelzer
Logical Innovations, Inc., Edwards, California 93523

Deborah R. Jackson, and Rachel J. Suitor
Universities Space Research Association, Edwards, California 93523

National Aeronautics and
Space Administration

Armstrong Flight Research Center
Edwards, CA 93523-0273

July 2021

Acknowledgments

Many people contributed directly to this work through their ideas, comments, suggestions, and assistance. The authors concede that many people are likely inadvertently omitted from the list below, and we express our apologies for any collective failures of memory. Our thanks to:
Derek Abramson, Chris Acuff, Jonathan Adams, Mike Agnew, Keenan Albee, Estela Bragado Aldana, Mike Allen, Luis Andrade, Sipanah Arutyunyan, Erin Askins, Dan Banks, Leo Banuelos, Josh Barrett, Sam Batarseh, Ryan Beattie, Nathan Bell, Dave Berger, Blake Berk, Robert Bloom, John Bodylski, Nathaniel Boisjolie-Gair, Olivia Bosma, Jason Bowen, Jesse Brady, Connor Bray, Jerry Budd, Andrew Burrell, Michael Butros, Dennis Calaba, Kimmie Calahan, Brent Cano, Donna Cedana, Johncarlo Cerna, Alex Chen, Kai Creason, Ethan Czuppa, Paul Dees, John Del Frate, Bryce Doerr, Ryan Dunphy, Dante Duran, Louis Edelman, Noah Edwards, Ana Escalera, Cynthia Farr, Nick Farrell, David Faust, Kirsten Fogg, Mike Frederick, Tomoki Fukazawa, Christian Gelzer, Katherine Glasheen, Scott Gleason, Emily Glover, Kevin Guerra, Jacob Gustafson, Eric Gutierrez, Etan Halberg, Justin Hall, Lydia Hantsche, Adam Harding, Stephen Harris, Ross Hathaway, Victoria Hawkins, Kira Headrick, Zack Hewitt, Bob Hoey, Brendan Holland, Sanel Horozovic, Reimar Horten, Walter Horten, Richard M. Howard, Lauren Hughes, Samantha Hull, Deborah Jackson, Chris Jensen, Jack Jensen, Taylor Jensen, Kristyn Kadala, Cody Karcher, Koen vander Kerckhove, Mike Kerho, Elizabeth Kissling, Emma Kleiner, David Kloesel, Kurt Kloesel, Michael Kloesel, Macie Kowalski, Brian Kramer, Heather Laffoon, Kyle Lanni, James Larson, Cameron Law, Joyce Le, Mandy Ledford, David Lee, Russell Lee, Jack Levine, Jay Levine, Caleb Lloyd, Victor Loera, Arlene Lopez, Joe Lorenzetti, Brooke Losey, Kyle Lukacovic, Paul MacCready, Justine Mack, Anthony MacPherson, Jose Manriquez, Mike Marston, Walker Martin, Ben Martins, Kassidy McLaughlin, Orlando Mielke, Chris Miller, Stephen Moes, Matt Moholt, Lesli Monforton, William Morris, Rick Motalwakel, Jim Murray, Hussein Nasr, Emma Neal, Loren Newton, Golda Nguyen, Gunhilde Horten Nickel, Karl Nickel, Eric Nisbet, Alexandra Ocasio, Dennis Olcott, Gary Osoba, Joe Pahle, Steve Parcel, Allen Parker, Kurt Pauer, Frank Pena, Shelby Pfeifer, Nancy Pinon, Joseph Piotrowski, Brian Plank, Ariel Prabawa, Bogdan Pugach, Andy Putch, Ronalynn Ramos, Nalin Ratnayake, Chris Regan, Nickelle Reid, Terry Reilly, Stephanie Reynolds, Rebecca Richardson, Jeromy Robbins, Amanda Roberts, Javier Rocha, Emma Ruano, Victor Ruiz, Aamod Samuel, Barkha Scherp, Peter Selinger, Jaiwon Shin, Alec Sim, Patrick Sosa, Amada Spakes, Reinhold Stadler, Marko Stamenovic, Alex Stuber, Curtis Stump, Rachel Suitor, Kaitlyn Summey, Ed Swan, Chante Swart, Josh Tanon, Brian Taylor, Carla Thomas, Jack Toth, Tom Tschida, Edward Uden, Julianna Plumb Ulrich, Eduardo Uribe-Saldana, Moiz Vahora, Felipe Valdez, Christos Valiotis, Lynn Valkov, Steffi Valkov, David Voracek, Abbigail Waddell, Joey Wagster, Megan Waller, Kaixi Wang, Shelby Worrell, Christine Yang, Hovig Yaralian, Seung “Paul” Yoo, Ivo Zell, and Jonathan Zur.

This report is available in electronic form at

http://sti.nasa.gov

Abstract

This report describes the validation of the 1933 Prandtl bell spanload. This spanload is the minimum induced drag of a wing for a given structural weight with properties that eliminate adverse yaw. Aircraft using the Prandtl bell spanload were flown and investigated. The results of this research show that many previously held assumptions should be rethought, and the creation of aircraft using the Prandtl bell spanload will require considerable new techniques.

Part of this work centered on the use of inverse methods. The usual first-step approach to a computational fluids problem is to create a geometry of the aircraft. Once this geometry exists, the computational fluids solution has been solved; however, the problem of creating the geometry still exists. A very small segment of the computational fluids world has concentrated on inverse solutions. This design approach begins with an end result - the computational fluids solution; from this end result, the geometry is sought.

A more generic inverse tool was desired that would allow for the design of wings - specifically Prandtl bell spanload wings. Such a tool has been developed and allows for variable taper, aspect ratio, sweep, airfoils, and design-lift coefficients; output from the tool results in twist distribution of wings.

Nomenclature

AOA	angle of attack
CG	center of gravity
dw	downwash
DE	elevator deflection
DUCP	downwash-upwash-crossover-point
EPM	electronic pressure measurement
FOSS	Fiber Optic Sensing System
L/D	lift/drag
MAC	mean aerodynamic chord
MIL	minimum induced loss
RMS	root mean square
RPM	revolutions per minute
UAS	unmanned aircraft systems
X_C	chord (inches)
2D	two-dimensional
3D	three-dimensional
C_D	coefficient of drag
C_L	coefficient of lift
C_m	coefficient of pitch moment
$C_{n\delta a}$	coefficient of yawing moment as a function of delta aileron deflection
C_p	coefficient of pressure
α	angle of attack

Introduction

On June 22, 1918 the esteemed professor Ludwig Prandtl stood before his students and began a derivation on the blackboard. His students took notes and two of them, Max Munk and Albert Betz, paid special attention. Prandtl had developed his lifting-line theory and was explaining his idea to his students. Prandtl would later translate these works into English; these works were published in 1918 (ref. 1) and 1919 (ref. 2).

Prandtl's lifting-line theory proposed that the lift of a wing can be formulated as equivalent to the circulation around a line. This became the first analytical tool by which the lift of a wing could be calculated. The tool also enables the estimation of the load experienced by the wing, allows for arbitrary planforms, arbitrary twist, and control surface deflections. Prandtl then extended the idea to calculate the minimum induced drag for a wing of a given wingspan. Prandtl showed this value to be the elliptical spanload (ref. 3), as shown in figure 1. In Prandtl's 1921 elliptical spanload is shown the extension of the elliptical spanload to the optimization of the propeller by Betz (see ref. 3). An extension of Prandtl's work (ref. 4) allows for the effects of multiple wings.

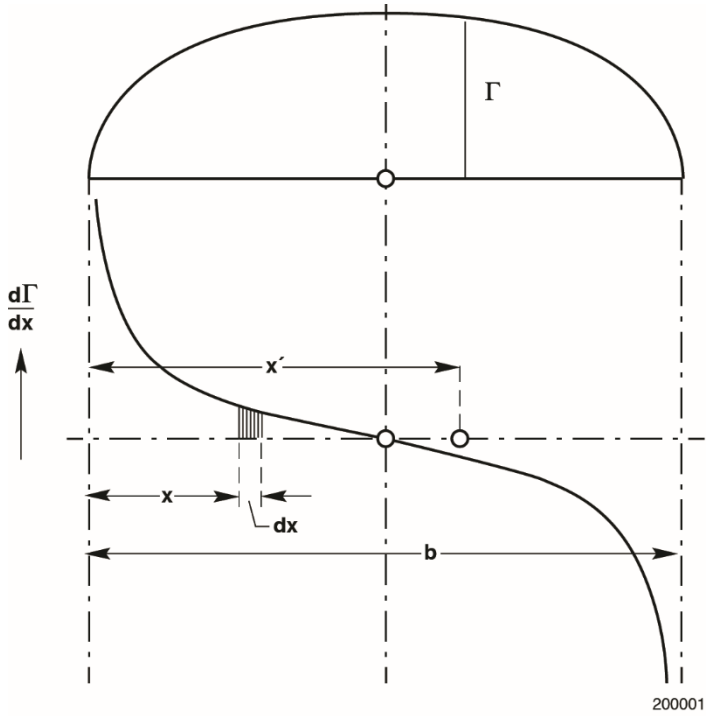

Figure 1. The 1921 Prandtl elliptical spanload.

Both the 1921 spanload by Prandtl and the 1921 propeller formulation by Betz were established using the wing span or the propeller diameter as constraints. In 1933 Prandtl created a newly optimized spanload (ref. 5). The new spanload is not elliptical and discards the span constraint. In its place is a structural constraint of holding constant the integrated root-bending moment of the wing. Figure 2 shows a comparison of the lift and downwash span distribution of the elliptical and bell spanloads with their respective integrated wing-root bending-moment held constant at the same value. The new spanload (which we refer to as being bell-shaped) has 22.5-percent more span and 11.9-percent less induced drag than the equivalent elliptical spanload. Recall that the elliptical spanload was presented by Prandtl in 1921 and produced the minimum induced drag for a given wing span. The bell spanload was presented by Prandtl in 1933 and produced the minimum induced drag for a given total structural weight of the wing.

When comparing Prandtl's two minimum drag solutions, it is important to remember the specific constraints that resulted in each one. The 1921 solution yields a minimum drag for a given wing span. The 1933 solution yields a minimum drag for a given weight of wing spar. By holding the mass of the

wing structure (the wing spar) constant, the span increases as the load near the wing tip is decreased to maintain the constant weight of the wing structure which has the effect of increasing the aspect ratio, therefore reducing the induced drag. The decrease in load near the wing tip has the effect of reducing the span efficiency which increases the induced drag. In the balance between these two effects the increase in the wingspan dominates, resulting in a net decrease in the induced drag.

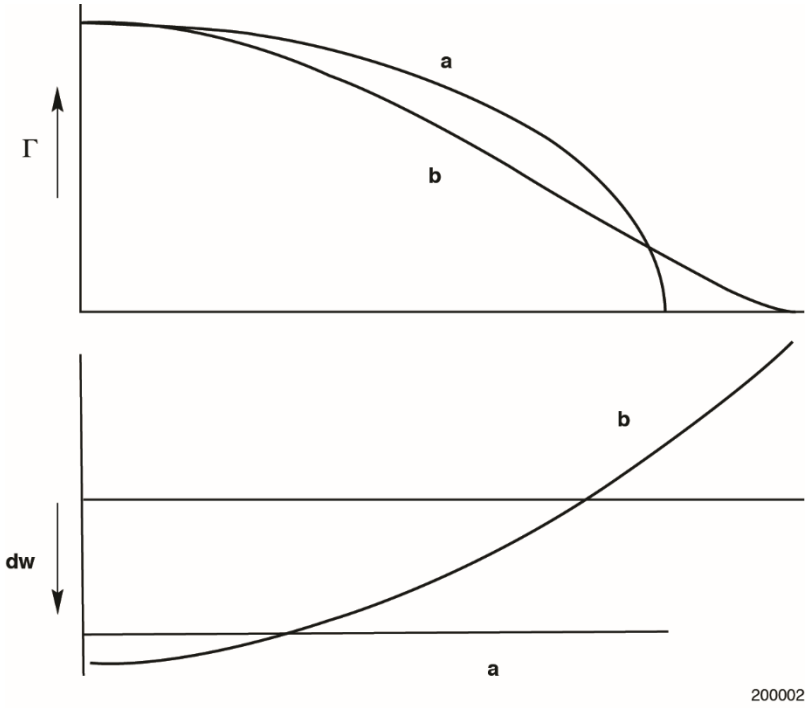

Figure 2. The Prandtl elliptical spanload (curve a) compared to the Prandtl bell-shaped spanload (curve b).

Other researchers have proposed alternative bell-shaped spanloads using differing constraints compared to Prandtl's bell solution. Starting in about 1935 the Horten brothers (refs. 6-8) designed and constructed a series of increasingly higher-performance sailplanes, and other aircraft, in a pursuit of proverse yaw (ref. 9) flight mechanics solutions. Ultimately, on the cusp of the discovery of the solution of this flight mechanics problem, Reimar Horten ceased his life's work in 1954, leaving the solution unproven. Horten never entered into the solution of the induced-drag problem. In 1950, researcher Robert T. Jones of the National Advisory Committee for Aeronautics (NACA) created a spanload that used the wing-root bending moment as a structural constraint (ref. 10) and found a related solution to that of the Prandtl bell spanload. Jones showed a 26-percent gain in span with a 17-percent reduction in induced drag (but allowed an unspecified small increase in structural weight). Finally, in 1975 the two researchers Armin Klein and Sathy Viswanathan (ref. 11) extended Prandtl's bell spanload by adding an additional constraint that used the shear of the wing (holding the integrated shear of the elliptical and bell spanloads constant). Klein and Viswanathan found that a 17-percent increase in span resulted in an 8-percent reduction in induced drag. This line of thought appears to end here and results in the refrain of Prandtl, Horten, Jones, and Klein and Viswanathan as the line of spanload researchers. Robert T. Jones (ref. 12) and Ilan Kroo (ref. 13) published collections of these differing thoughts, yet neither of them included Horten, indicating Horten's lack of tackling induced drag.

The solution to the spanload problem that solves the discrepancy between the flight of nearly all modern aircraft and the flight of birds affirms Horten's relevance to Prandtl, Jones, and Klein and Viswanathan. Only through the connection between the proverse yaw flight mechanics solution to the

adverse yaw problem and the minimum induced drag with the structural constraint solution, can one solve the bird flight spanload problem.

We selected the Prandtl solution for two reasons: one analytical and the other anecdotal (see ref. 9). The analytical reason is the formulation of the Breguet Range Equation (ref. 14) which shows that the range of an aircraft is equal to the propulsive efficiency multiplied by the aerodynamic efficiency, multiplied by the log of the quotient of take-off gross weight and landing weight (most of the landing weight is the structural weight) and then multiplied by a constant (to make the units work out correctly). Of note is the aerodynamic efficiency divided by the log of the landing (structural) weight. Kuchemann makes note of this solution (ref. 15), yet Kuchemann does not reference Breguet. This lack is one argument in favor of both Prandtl bell, and Klein and Viswanathan, solving for both induced drag and minimum structure. Anecdotal evidence would show that aircraft wings fail in bending and do not normally fail in shear. This argument favors the Prandtl bell and Jones spanload solutions, solving for both minimum induced drag and wing bending moment. The overlap between these two sets is the Prandtl bell-shaped lift distribution.

The downwash equation for the Prandtl bell-shaped lift distribution is a smooth, continuous function. Mathematically, a smooth continuous function is desirable because it eases manipulation. Singularities (points at which the mathematics go to infinity or degenerate (the equation does not produce an answer)) are intractable. The downwash calculation for the elliptical wing produces singularities at the wingtips, as shown in figure 3(a). Singularities exist in neither the spanload nor the downwash calculations for the Prandtl bell spanload, as shown in figure 3(b).

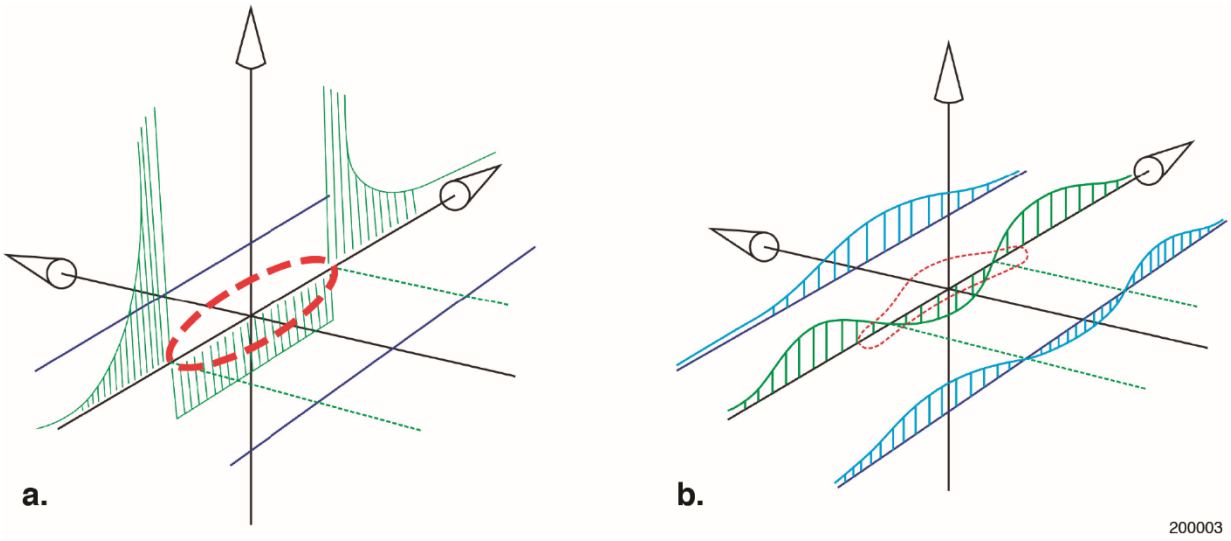

Figure 3. (a) The 1921 Prandtl elliptical spanload, with singularities (the upwash values approach infinity as the flow approaches the wingtips); and (b) the 1933 Prandtl bell-shaped spanload, with no singularities in the upwash/downwash flow field.

The increased complexity of the flow field demands an expanded definition to properly describe the flow around these wings. The classical elliptical wing is simple: the upwash (and the resulting downwash) is constant across the entire wing. A simple summation of the upwash and downwash thus could be made at any point along the wing, with the result always valid simply because the elliptical spanload produces completely uniform upwash and downwash across the entire wing. The Prandtl bell-shaped spanload, however, does not behave in this manner: it is a completely three-dimensional (3D) flow field solution. The result is that a simple solution no longer suffices; it is necessary to integrate the solution across the entire span of the wing to properly evaluate the total net downwash behind these wings.

“Wash” is the generic term for both upwash and downwash. Upwash is defined as a positive value; downwash is defined as a negative value, as shown in figure 4. The local upwash/downwash is the flow angle resulting from the immediate upwash or downwash at or near the leading- or trailing-edge across

the chord at a given span. The net upwash/downwash is the sum of the local upwash and local downwash across the chord at a given chord (or at a particular spanwise) location, as shown in equation (1). The total upwash or total downwash is the integrated value of the net upwash and the net downwash across the entire span of the wing, as shown in equation (2).

$$\textbf{Net}\ \text{upwash/downwash at a particular span location} = \Sigma\ [\textbf{Local}\ \text{upwash} + \textbf{Local}\ \text{downwash}] \tag{1}$$

$$\textbf{Total}\ \text{upwash or downwash} = \int \textbf{Net}\ \text{upwash + downwash} \tag{2}$$

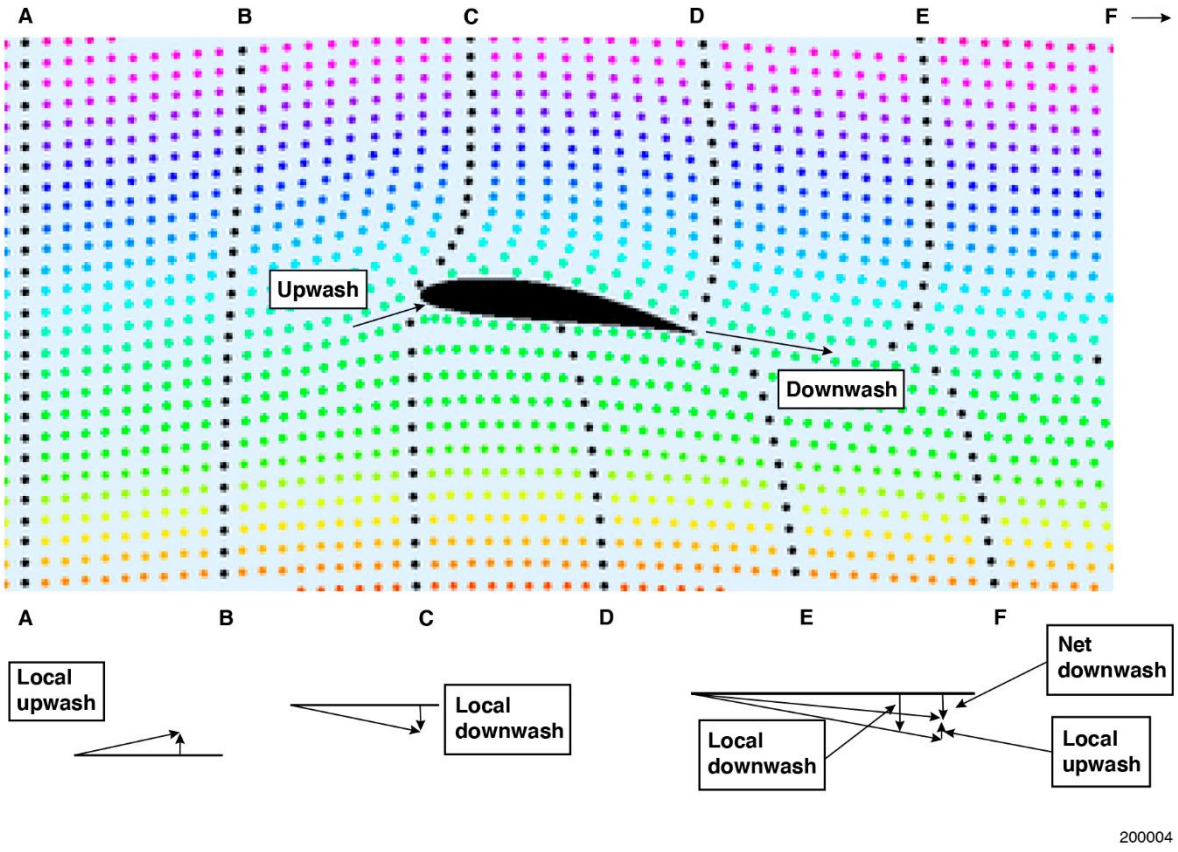

Figure 4. Local downwash, local upwash definition, and net upwash/downwash at a particular chord (spanwise location).

Prandtl's original formulation of the 1921 elliptical spanload was made in the following way. The solution is inviscid, so the effects of Reynolds number do not apply in the lifting-line formulation. The wing is assumed to be flat and is treated as a thin airfoil with no camber. The local upwash and the local downwash are the same for the entire span, the local downwash being of greater magnitude than the local upwash. Thus, the total effect of the wing is that the wing creates a net total downwash. In effect, the solution for the 1921 Prandtl elliptical spanload is that the flow is always a two-dimensional (2D) solution. The local lift coefficient is exactly identical at every point along the span, the local upwash is exactly identical at every point along the span, the local downwash is exactly identical at every point along the span, and the net downwash is exactly identical at every point along the span.

Contrast the 1933 Prandtl bell-shaped spanload. At the center, the local downwash overwhelms the local upwash; as a result, a net downwash exists at the centerline. This condition exists from the centerline out to the 70.7-percent span location, where the local upwash and the local downwash are equal, so the net downwash/upwash is zero. Outboard of the 70.7-percent span location, the local upwash is greater than the local downwash, so a net upwash exists all the way out to the wingtip. An integration of the net downwash/upwash curve will show a total downwash overall. In comparing the 1921 elliptical spanload total downwash to the 1933 Prandtl bell-shaped spanload total downwash, the induced drag is less for the bell-shaped spanload by 11.87 percent, compared to the elliptical-spanload induced drag.

The development of the elliptical spanload was created in the following way. The wing planform is elliptical, there is no twist, and the upwash is uniform along the entire leading edge. The downwash is uniform along the entire trailing edge. At every angle of attack (all of those angles that do not have separation anywhere on the wing) the wing will generate a constant net downwash everywhere behind the wing. Thus, the spanload is always elliptical. This approach led to the creation of the elliptical spanload. Effectively, the elliptical spanload is an imposed 2D solution onto the 3D wing.

This formulation fails very close to the wingtip. The real viscous fluid prevents the upwash from simply going to infinity, and the fluid simply creates an irrotational core to the vortex that shortcuts the downwash line to upwash curve across the wingtip. This irrotational core causes disruption in the airfoil flow, and the corresponding pressure distributions will not match the 2D solutions that panel methods or Euler solutions generate. Only full Navier-Stokes solutions have any hope of accurately capturing the flow fields and the airfoil pressure distributions near the wingtips.

The Betz formulation of minimum induced loss (MIL) for propellers is similar to the formulation of the elliptical spanload by Prandtl and Munk. Betz calculated the constant “inwash” for the propeller through the actuator disk. If you treat the propeller blade as a wing, inwash is the airfoil downwash. With a constant inwash, the upwash was held constant across the entire span of the propeller blade. The downwash was held constant as well. This condition dictated that the lift coefficient was held constant everywhere; the angle of attack was held constant along the entire blade span as well. The result is that the blade describes an almost perfect cut through the fluid with a constant angle of “slip” at all points along the blade.

It is necessary to use twist to create the Prandtl bell-shaped spanload. The twist is not a scalar quantity, it is a vector, and has both a direction and a variation in magnitude along the span. Prandtl’s 1933 paper states that the spanload can be achieved using planform “rather the lift distribution of a sharp-tipped wing”. The twist is necessary because of the twisted airflow across the span of the wing. The flow distribution is truly a 3D solution.

An analogy description used is a boat on a lake. Imagine a glass-smooth lake and a powerboat sitting on the lake. As the powerboat begins to move forward, a bow wave is formed. The bow wave rises above the level of the lake water. The powerboat is not directly pushing the water up, forming the bow wave, but is pushing the water down beneath the hull. The pressure disturbance in the water, caused by the powerboat, is creating the bow wave. Imagine two surfboards are surfing on the bow wave; both surfboards are moving forward at the same velocity as the boat. Now outriggers are added to connect the surfboards to the boat, and the surfboards are placed such that they are helping to push the boat forward a little bit. This description is a direct analogy for the Prandtl 1933 bell-shaped spanload solution. (Additionally, we can now steer the powerboat by pushing the bow of the powerboat boat to the left and to the right using the surfboards.)

Discussion

A small research project was built around the Prandtl bell solution. Four series of aircraft have resulted: three small unmanned aerial vehicle (UAV) series and a larger piloted aircraft. The small UAVs were created for the original flight mechanics investigation (those vehicles were called the Prandtl-D1 glider and the Prandtl-D2 glider, starting in 2011); the aerodynamics investigation (these vehicles were called the called Prandtl-D3 and the Prandtl-D3c, starting in 2014); and the Mars glider application (that

vehicle was called the Preliminary Research Aerodynamic Design to Land on Mars, or Prandtl-M). There exists, as well, the large glider called Prandtl 4.

Part of the development of this work involved the use of inverse methods. The usual approach to the computational fluids problem is to create a geometry of the aircraft. Once this geometry exists, the computational fluids solution can be found; however, this leaves the challenge of creating the geometry. Starting in the 1930s and progressing through the 1980s, a very small segment of the computational fluids world concentrated on inverse solutions. This thought process design approach begins with the idea of what the flow must look like in the end. Many selected simplifying assumptions must be made so that the mathematical solution to the inverse problem is tractable. The beauty of this approach is that the endpoint is the beginning. The difficulty lies in ensuring that the simplifying assumptions do not negate the validity of the final solution.

During these years, the forward method iterative approach was used. At the same time, it was known there existed an inverse method by which to design wings (see ref. 8). The inverse approach was very abstract and was only applicable to Horten spanloads. Also known was Horten spanloads and the Prandtl bell-shaped spanload had different constraints and resulted in different spanloads. A more generic inverse tool was desired that would allow the design of wings, specifically Prandtl bell-shaped spanload wings. Such a tool was developed and allowed variable taper (or variable chord length distribution), aspect ratio, sweep, airfoils, and design lift coefficients. The output of the tool is the twist distribution; however, the tool can also be inverted easily so that any of the other inputs can be made into the output. The beauty of this tool is that the spanload is the initial condition for the wing design. The difficulty is that the simplifying assumptions (lifting line and thin airfoil) do not negate the final wing solution. This report is the validation of the Prandtl bell-shaped spanload and this inverse tool.

The Prandtl-D1 glider (shown left in figure 5); and the Prandtl-D2 glider (shown right in figure 5) each had a wing span of 12.5 ft wing, a wing area of approximately 10 ft^2, and a weight of approximately 14 lb. Flight speed was approximately 45 ft/s. These aircraft were instrumented strictly for flight mechanics. There were 12 parameters measured: angle of attack, angle of sideslip, total pressure, static pressure, pitch rate, roll rate, yaw rate, normal acceleration, axial acceleration, and lateral acceleration, left elevon deflection, and right elevon deflection.

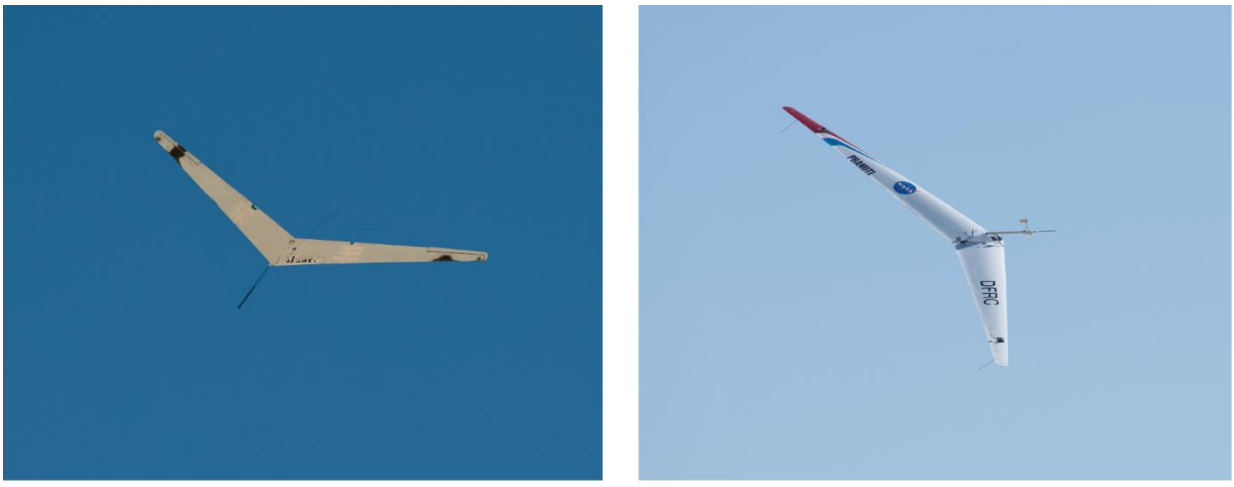

Figure 5. (left) The Prandtl-D1 glider in flight; NASA photograph number ED13-0061-39; and (right) the Prandtl-D2 glider in flight; NASA photograph number ED13-0279-54

The Prandtl-D3 and Prandtl-D3c gliders each had a wing span of 25 ft, a wing area of approximately 40.5 ft^2, and a weight between 28 lb and 64 lb. Flight speeds were approximately 26 ft/s to 40 ft/s. The variation in weight was due to the particular experiment being flown. The Prandtl-D3 glider, shown on

the left in figure 6, weighed as little as 28 lb for flight mechanics experiments. The Prandtl-D3c glider, shown on the right in figure 6, weighed approximately 64 lb for the Fiber Optic Sensing System (FOSS) experiments; for the wing pressure experiments the Prandtl-D3c glider weighed approximately 45 lb.

Figure 6. (left) The Prandtl-D3 glider in flight; NASA photograph number ED15-0330-079; and (right) the Prandtl-D3c glider in flight; NASA photograph number AFRC2018-0182-34.

The Prandtl-D4 glider, shown on the left and right in figure 7, is a piloted single-seat glider with a wing span of approximately 50 ft, a wing area of 162 ft^2, and weight of approximately 150 lb empty.

Figure 7. (left) The Prandtl-D4 glider on the ground; and (right) the Prandtl-D4 glider in flight.

The Prandtl-M glider, shown in figure 8, utilizes the research obtained by the Prandtl-D gliders to create a glider that is planned to be released in the Martian atmosphere from a 3U CubeSat (California Polytechnic State University, San Luis Obispo, California) to fly at Mach 0.5 and collect atmospheric and cartographic data. There are currently two models being tested, called the Prandtl-M (PM) 4.2 and PM 5.0. The PM 4.2 has a wing span of 31.25 in, a wing area of 250 in^2, and a weight of approximately 0.4 lb. The PM 5.0 has a wing span of 24 in, a wing area of 144 in^2, and a weigh of approximately 1.16 lb.

Figure 8. The Prandtl-M glider in flight.

Results

Recent work falls into three categories: (1) flight mechanics work, as an update to the previous flight mechanics work (see ref. 9); (2) Fiber Optic Sensing System in-flight structural loads to find the spanload; and (3) integrated pressure measurement over the wing to find the spanload. The FOSS fibers and the wing pressures are diagrammed in figures 9(a) and 9(b). Other work included extending the approach to propellers and fans.

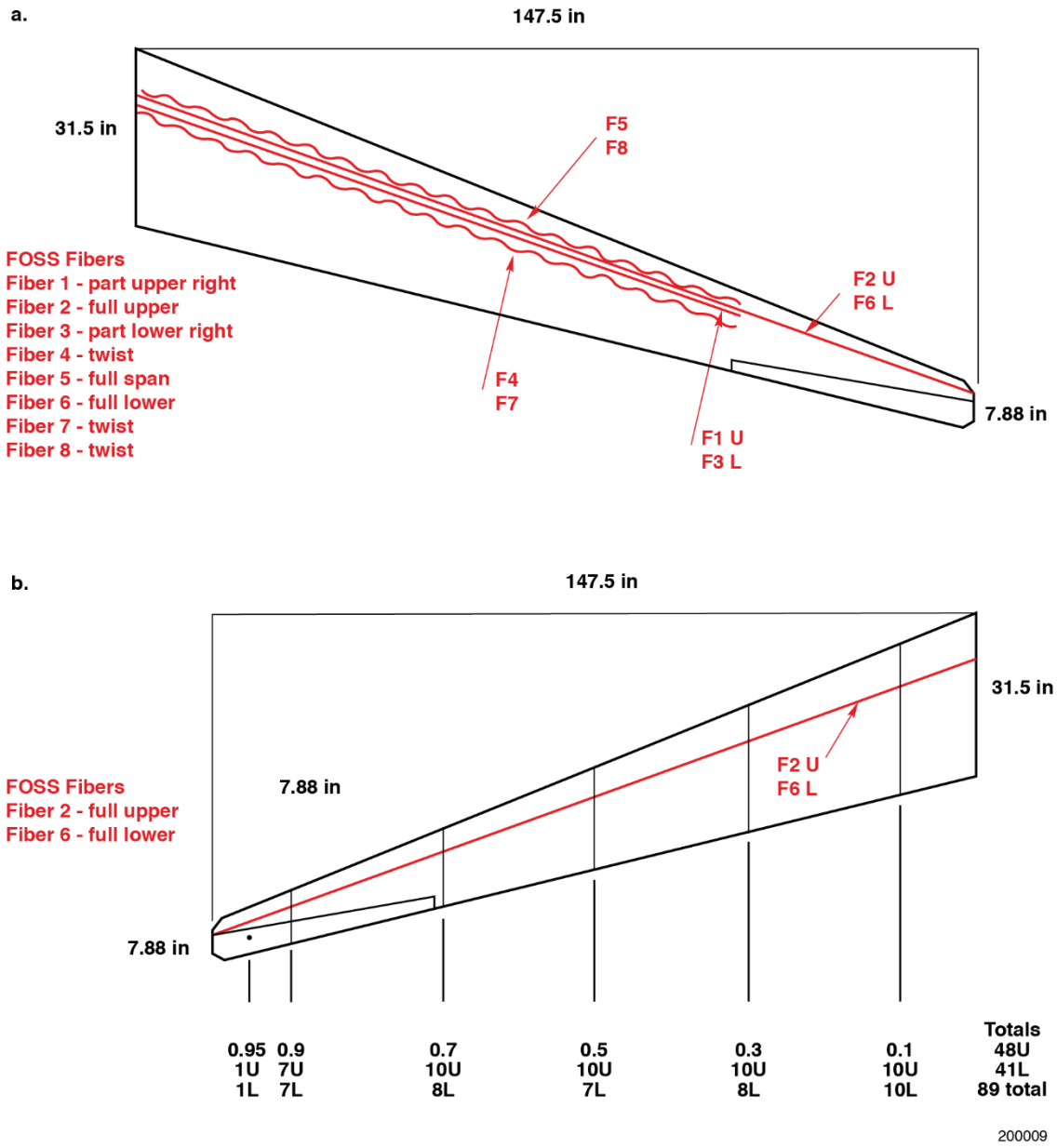

Figure 9. (a) The Fiber Optic Sensing System fiber installation in the right wing; and (b) wing pressures and Fiber Optic Sensing System fiber installation in the left wing.

Flight Mechanics

The flight mechanics work was continued on the gliders previously described (see ref. 9). As part of this work, identical data sets were used by two teams comprised of student interns; independent analyses were conducted using the same tools and similar, though not identical, techniques (different weightings for parameters were selected by each team). The parameter estimation technique used (ref. 16) has been shown to provide robust and accurate results. Cramer-Rao uncertainties are output as well. The linear fits shown are based on vortex-lattice (ref. 17) estimates of the control power parameters and estimates from those results for the stability and control derivatives for comparison. The two teams each used the inverse of their own uncertainty estimates as weightings for the linear equation fits for the stability and control parameter for proverse or adverse yaw with aileron deflection. The parameter, $C_{n\delta a}$ (coefficient of yawing moment as a function of delta aileron deflection) is a measure of proverse or adverse yawing moment

with aileron deflection. A positive $C_{n\delta a}$ indicates there is a proverse yawing moment with aileron, that is, the aircraft will roll and yaw in the desired direction as commanded by the pilot. Should the value be negative, there exists an adverse yawing moment with aileron deflection, so the roll and yaw are opposite to each other and adverse yaw exists. The three results are plotted for comparison in figure 10.

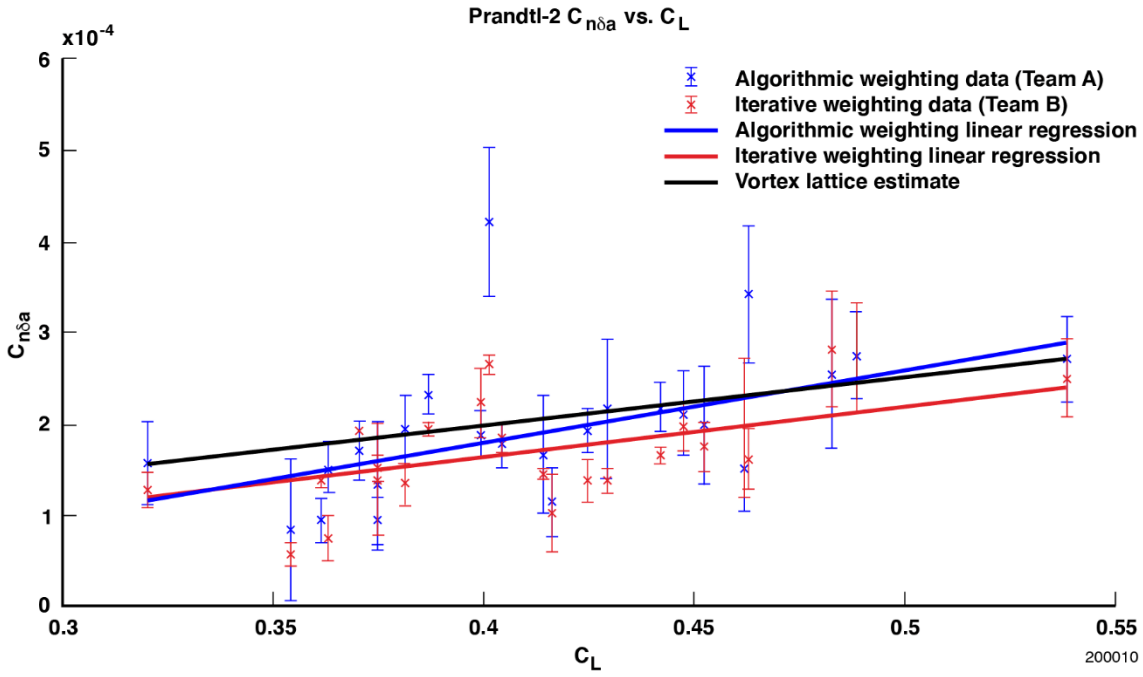

Figure 10. $C_{n\delta a}$ (coefficient of yawing moment as a function of delta aileron deflection). Black vortex lattice prediction. Blue Team A estimates of $C_{n\delta a}$ from flight data. Red Team B estimates of $C_{n\delta a}$ from flight data.

Fiber Optic Sensing System

The FOSS system, shown in figure 11, (ref. 18), was designed into the Prandtl-D3 and Prandtl-D3c gliders. Using the FOSS system allowed insight into the actual spanload exerted on the aircraft, as well as being a validation of the inverse wing design methodology. The FOSS, an experimental and extremely promising technology, is shown in figure 11.

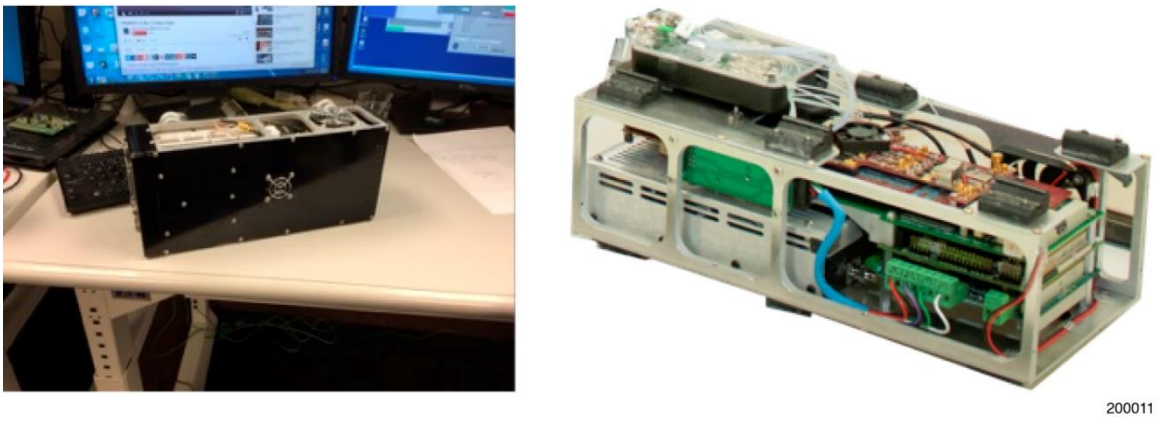

Figure 11. The Fiber Optic Sensing System.

The principle experiment with FOSS was concentrated on the right wing. A set of fibers was glued into the surface of the wing skins, both upper and lower, near the spar. The fibers make use of a pulsed laser that directly measures strain (compression and tension) during flight. The fibers use a Bragg grating every 1 cm and record the fiber and grating data at 100 samples per second, as shown in figure 12.

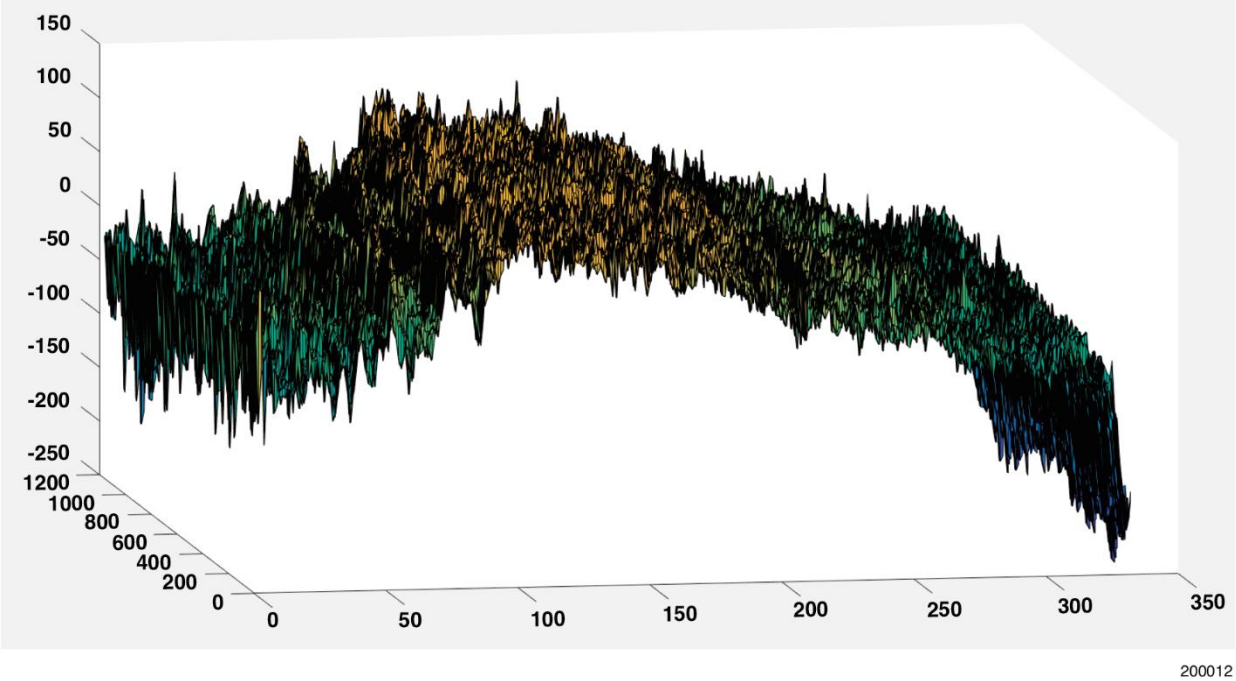

Figure 12. The Fiber Optic Sensing System data from a 12-s slice. The wing root is at the left side of the three-dimensional graph; the wingtip is at the right side of the graph, and time progresses into the page. This data set comprises approximately 400,000 data points.

Because of the relative effects of derivation and integration, the numerical noise that exists in digital systems is either filtered out (and the resulting data are incredibly smooth) or the effects of the noise are augmented, resulting in data that are difficult to work with. Ideally, with perfect data, the results would appear as represented in figures 13(a), 13(b), 13(c), and 13(d).

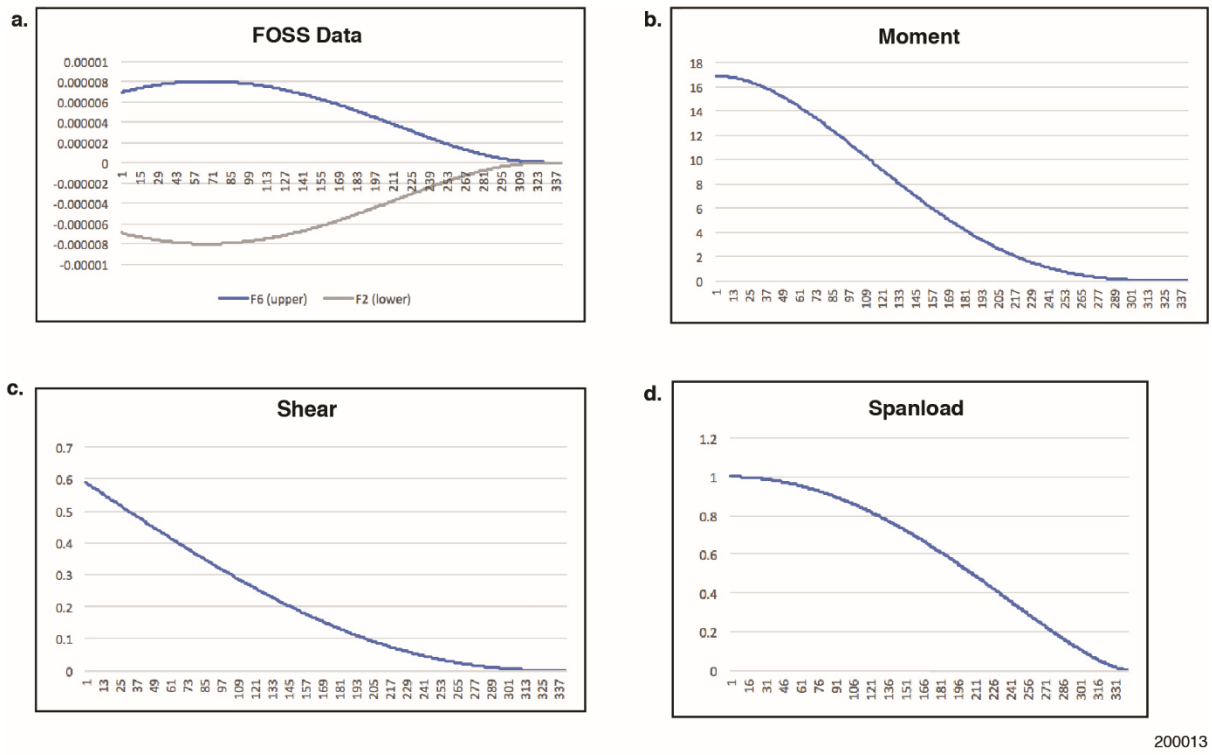

Figure 13. (a) Ideally, the Fiber Optic Sensing System data would look like this: the lower surface on top (under tension so positive strain) and the upper surface on bottom (under compression so negative strain); (b) moment is generated by the geometry of the wing and the mechanical structural properties, and shown is the total moment difference between the upper and lower surfaces; (c) shear is the result of differentiating the moment; and (d) the spanload is a result of differentiating the shear. This spanload is the ideal Prandtl bell spanload.

The real FOSS data required smoothing of the data to prevent the differentiation from propagating off to infinity (this process is often called “blowing up”). The real data required some care in smoothing, as shown in figures 14(a), 14(b), 14(c), and 14(d).

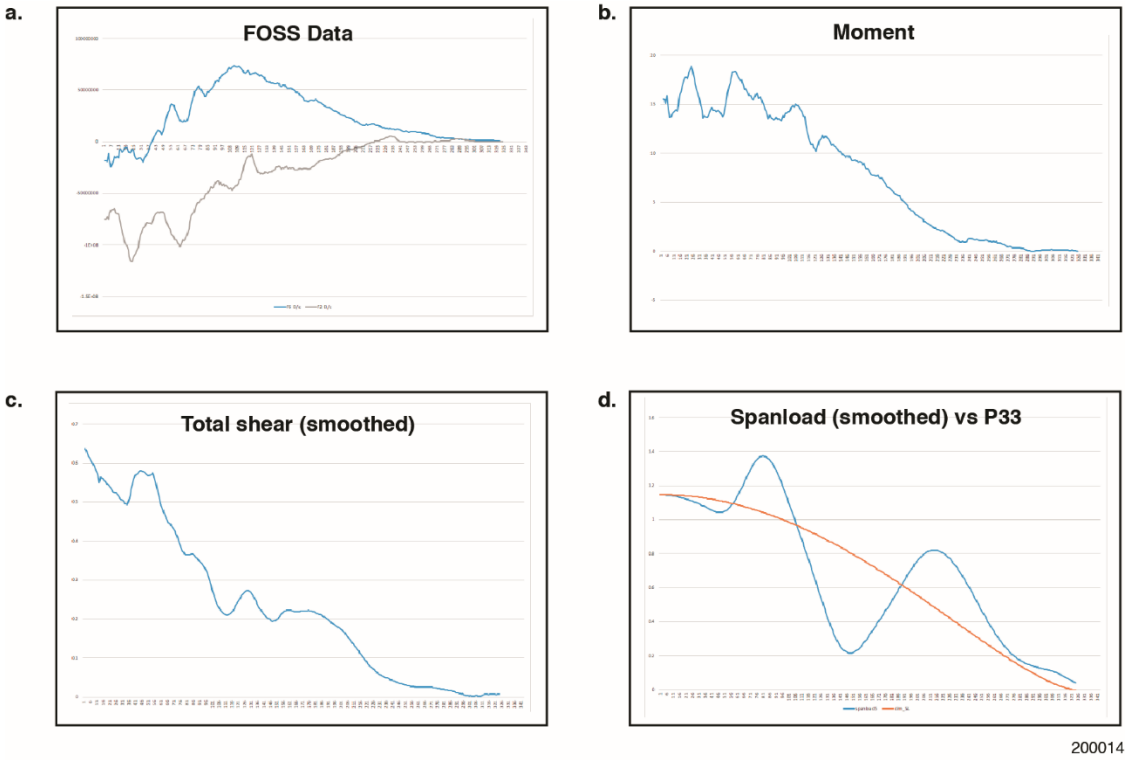

Figure 14. (a) Real Fiber Optic Sensing System data from the fibers on Prandtl-D3c; the lower surface on top (under tension so positive strain) and the upper surface on the bottom (under compression so negative strain): the lower surface (blue line) is the data used from figure 6; (b) total moment data based on the measured wing geometry, the estimated material properties, and the data gathered in flight from the Fiber Optic Sensing System data; (c) differentiating the moment data results in the estimated shear. The raw shear data was very noisy, and filtering was required. Shown here is the filtered estimated shear; and (d) differentiating the shear data results in the estimated spanload. The raw spanload data was very noisy and filtering was required. Shown here is the filtered estimated spanload (blue), plotted over is the ideal Prandtl 1933 (P33) bell spanload by Prandtl (orange).

The integration to find the wing deflection results in a very smooth curve. In preparation for the wing deflection data, a calibration proof test was performed. The aircraft configuration was approximately 64 lb with the FOSS system installed. The wing was loaded with 64 lb of sandbags at six span locations (three on each wing). The loading was approximately equivalent to that of the Prandtl bell-shaped spanload. Wingtip deflections were measured both fully loaded and unloaded. The wing tip deflections were found to be approximately 4.25 in at the full 1-g load.

The FOSS system flights were flown in the late summer of 2017. The FOSS system gathers data independent of the flight mechanics data system. Time correlation of the data sets is not difficult. The launch technique resulted in an immediate 3-g axial load on the glider, and the landing pulse provided a like spike in the normal accelerations. Both these events provided very accurate event markers for both data systems. The FOSS data were downloaded after each flight. A suitable flight very close to the design point of the glider (lift coefficient $C_L = 0.6$) is shown. The microstrain was correlated to the wing deflection measurements taken during the proof calibration test (figure 9). The microstrain was 215,550 microinches at the tip. The data corresponded to 4.31-in deflection at the tip, as shown in figure 15.

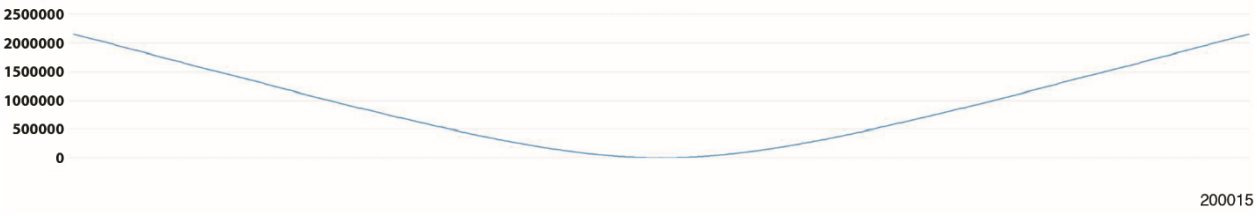

Figure 15. Estimated wing deflection in bending from in-flight Fiber Optic Sensing System data (1-g non-maneuvering level flight).

Wing Pressures

In addition to the FOSS research, direct aerodynamic measurement of the spanload was also pursued. To this end, the left wing of the aircraft was instrumented. Eighty-nine flush pressure ports were 3D printed and installed in five rows built into the wing, plus two individual ports near the tip, as shown in figures 16 (left, center, and right). These pressures were to measure the local lift at each individual pressure row and then integrated to produce the spanload distribution for comparison to the Prandtl bell-shaped spanload.

Figure 16. (left) External view of the three-dimensional printed flush pressure ports (row 4); (center) internal view of the three-dimensional printed flush pressure ports (row 4); and (right) internal view of the flush port installed in the elevon control surface with tubes attached.

Special instrumentation was created, called the Electronic Pressure Measurement (EPM) box. The instrumentation was designed, built, and tested by student interns. The box used individual "smart" pressure transducer sensors, all of which required microprocessor interrogation. BeagleBone® Black (BeagleBoard.org, Oakland Township, Michigan) microcomputers were used to operate the pressure transducers. Each BeagleBone® Black operated 32-pressure transducers, all of which were contained on custom cards designed and fabricated by the student interns. Three cards were contained in the EPM box, shown in figure 17. A Raspberry Pi "Raspberry Pi is a trademark of the Raspberry Pi Foundation" microcomputer (Raspberry Pi Foundation, Cambridge, United Kingdom) was used to record the data from each card set and data was then written to a Secure Digital (SD) card (non-volatile memory). In the event of a power interruption, the data were preserved on the memory card.

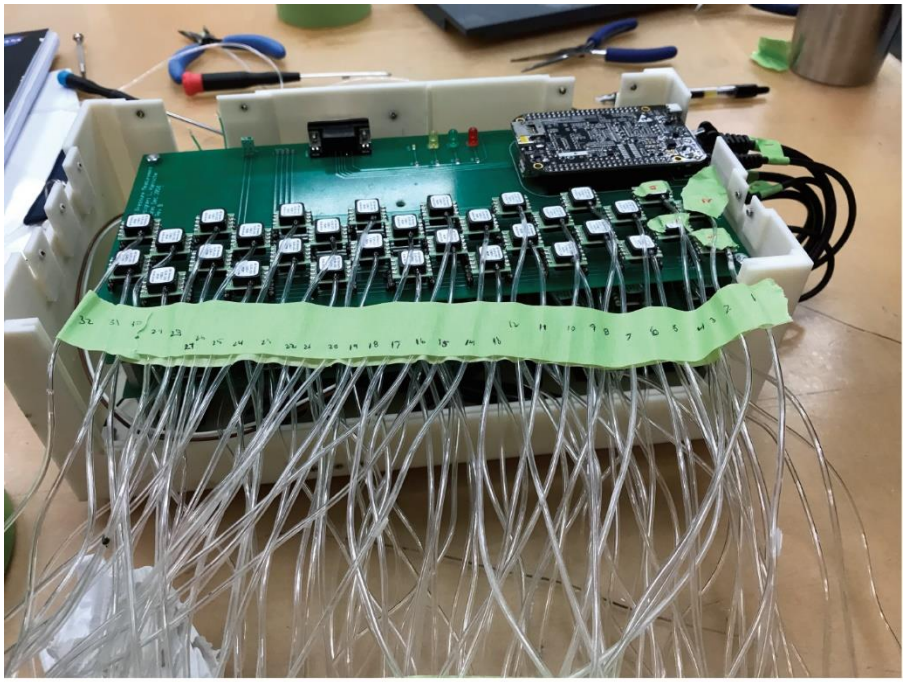

200017

Figure 17. The Electronic Pressure Measurement Box.

Calibration of the pressure transducers was necessary to ensure accurate pressure measurement. In the past, the use of pressure transducers was difficult due to the response of traditional equipment. Considerable amounts of noise created problems for low-speed, low-dynamic pressure applications. The advent of modern microprocessor-controlled transducers promised more accurate data from modern devices. Initial tests were not so promising. Using the manufacturer supplied calibrations showed some variation that would create problems with flight measurement of the pressure profiles over the wing. The student interns were undaunted and proceeded to accurately recalibrate each pressure transducer. Their efforts showed particular promise, as shown in figures 18(a) and 18(b).

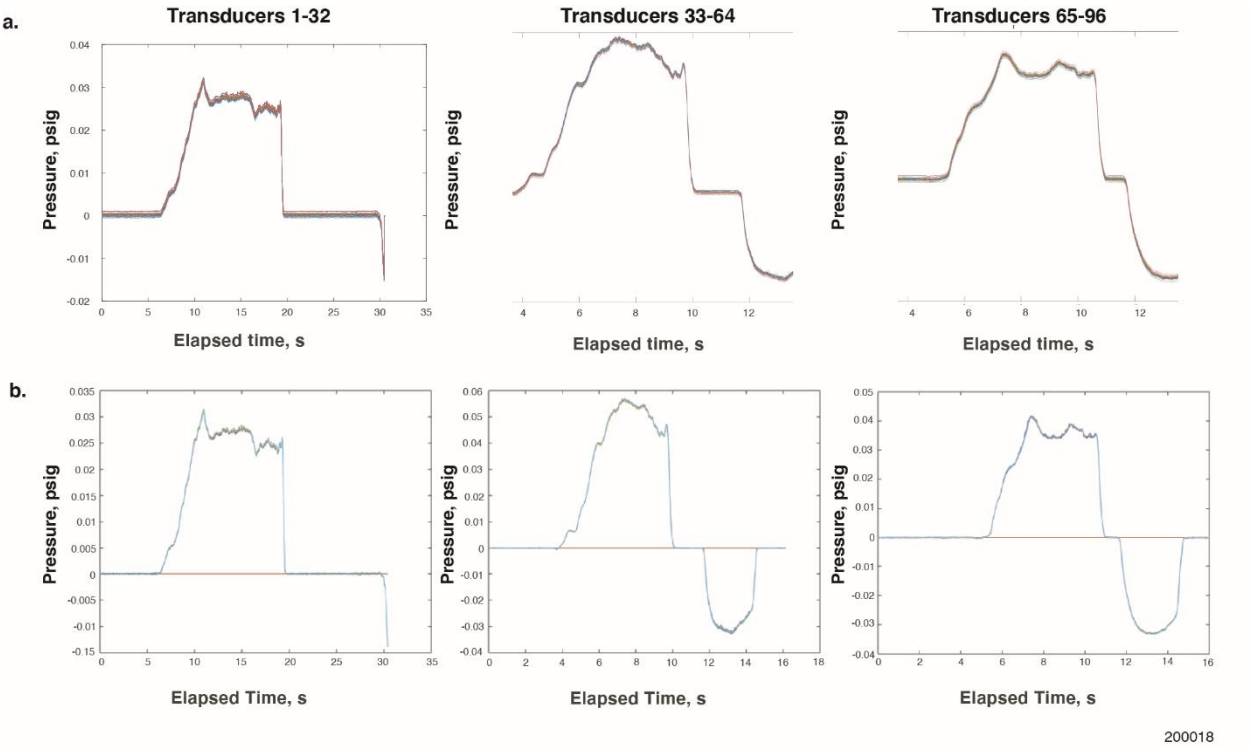

Figure 18. (a) (left, center, and right) Pressures from cards with 32 pressures each using original pressure calibrations; and (b) (left, center, and right) pressures from cards with 32 pressures each using the updated calibrations.

The updated pressure traces were remarkably accurate compared to what previous systems had yielded, and under considerably reduced dynamic pressures compared to previous wing pressure experiments. The pressure system worked well, and necessary data was gathered. From the data, pressure distributions were made, as shown in figure 19.

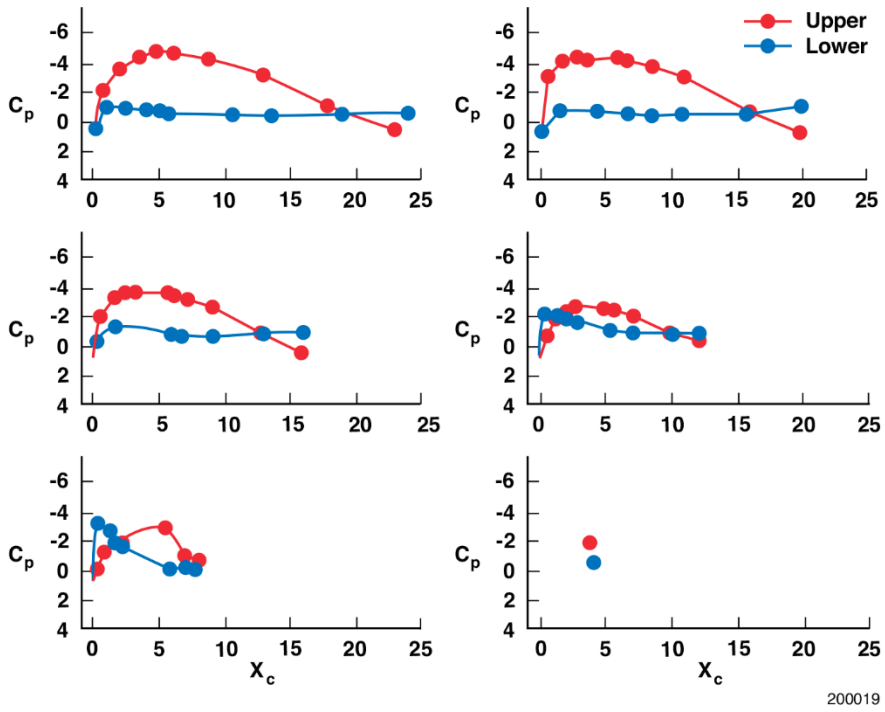

Figure 19. Pressures measured in flight from the wing. Red is the upper surface; blue is the lower surface. Vertical axes are C_p (coefficient of pressure); horizontal axes are chord in inches. The (upper-left) profile is the 0.1-span chord; and (upper-right) is 0.3 span; (center-left) is 0.5 span; and (center-right) is 0.7 span; (lower-left) is 0.9 span; and (lower-right) are the individual ports at 0.95 span.

By averaging the coefficients of pressure and integrating the respective profiles it is possible to find the spanload of the aircraft during flight. Two remaining pieces of information are needed prior to viewing the results of the flight data. The pilots preferred the center of gravity (CG) to be slightly forward of the design point. As a result of this slightly forward CG, we were forced to carry a fraction of up-trim in the elevons; the up-trim would affect the spanload results. In 1996, vortex lattice was used (see ref. 17) to predict the results of the trim on the spanload, as shown in figure 20.

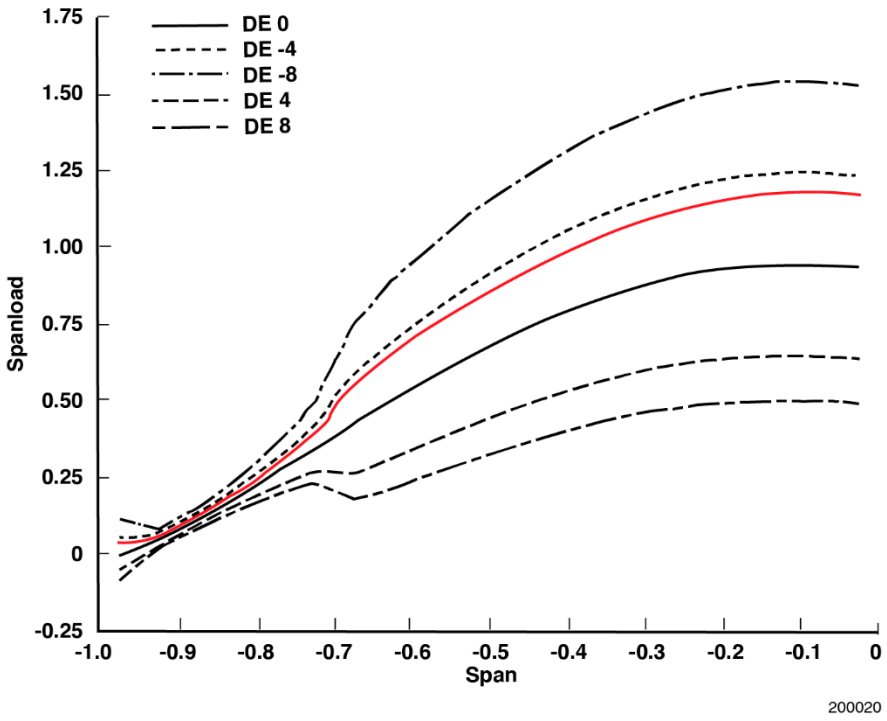

Figure 20. Effect of trim on the spanloads. Red line for spanload with peak C_L=1.16.

The red line peaks at C_L=1.16, which is a flight condition for which we had flight data. The flight data for this same condition follow, as shown in figure 21.

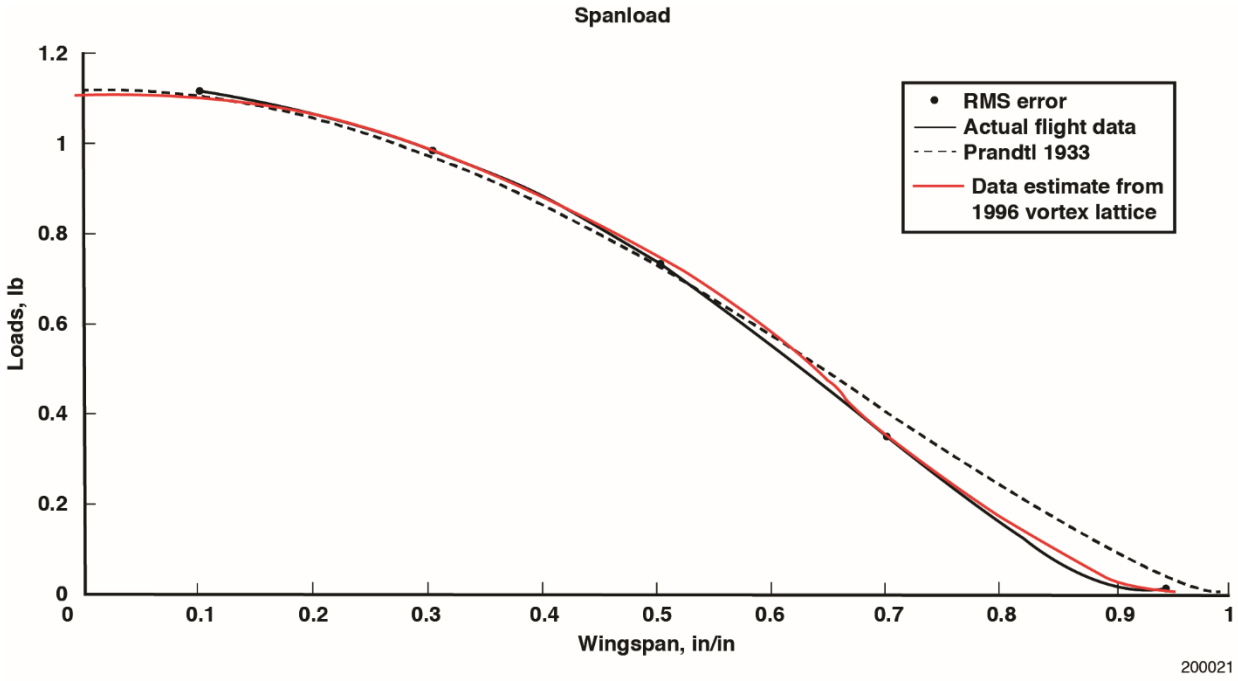

Figure 21. Comparison of measured flight data spanload (solid black line with dots); the 1996 estimate of spanload with trim to attain peak at C_L=1.16 (red line); and Prandtl bell spanload (dashed line).

Propeller

An extension of the ideas generated by Prandtl's approach to the bell-shaped spanload was extended to propellers. If such a solution could be found, implicitly it might mean that propellers, rotors, impellers, compressor blades, and fans would also benefit by the same means. Also implied, though less directly, is the design of turbines.

The thought experiment begins in the following way: if propulsion is treated as a black box, then the only important things are the input and the resulting outputs. What is inside the black box does not matter, only that the desired result comes out of the black box. In this case, power is put into the black box and thrust is what comes out.

Propellers are rather different than wings. There is a very strong span constraint with propeller blades: diameter. As arbitrary constraints, the blade planform and revolutions per minute (RPM) (angular rotation rate) were also held constant. The remaining free design parameter is the twist of the blade.

One prominent constraint that was discarded was the minimum induced loss (MIL). The MIL has been used in the design of propellers since at least 1921, when it was first introduced (see ref. 3). The MIL is not the same as the minimum energy solution for propellers. The MIL simply means that each blade element is optimal at its respective radius. As a consequence, the MIL propeller has not been optimized in any global sense but only for each radii of the blade.

If RPM is held constant, then the remaining output for which the optimization is done is to find the minimum torque. With constant RPM, minimizing torque will result in the minimum power required for a given thrust output.

What would such a propeller look like? In the first pass at the optimization (2012) the resulting curve looked odd, as shown in figure 22.

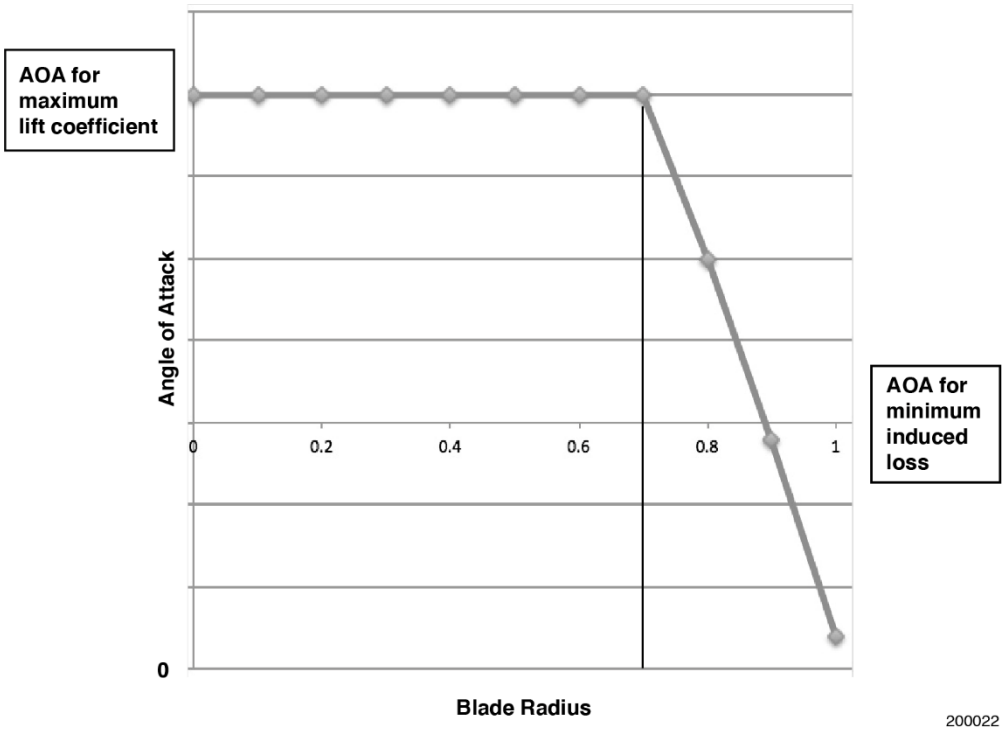

Figure 22. Diagram of angle of attack versus blade radius.

A subsequent effort was made; two small adjustments were found to improve performance, as shown in figures 23(a) and 23(b).

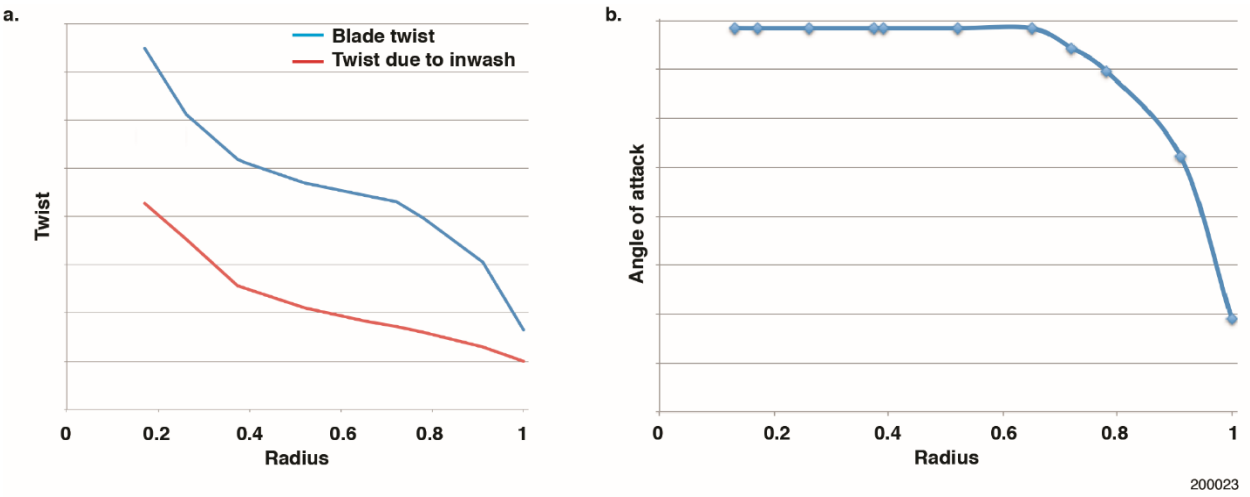

Figure 23. (a) Curves of the twist required for the blade (red) and the resulting inflow (blue); and (b) angle of attack required for the blade.

The new propeller blade requires a maximum lift coefficient from the root out to a particular breakpoint in radius, after which the angle of attack is "rolled-off" to a much-reduced angle of attack value at the tip. The resulting blade has a dramatically reduced torque (approximately 15 percent) for the same thrust.

In designing blades for these solutions, the blade is a cambered airfoil from the root to the breakpoint, and then the airfoil is blended into a more symmetric airfoil. By extension, such an airfoil may be able to operate with increased tip speeds compared to what is normally used for propellers because the unloaded tips would be less subject to shock problems.

An additional side effect of blades made in this manner would be a reduced noise signature. The unloaded tip has the effect of reducing the large shear layer intensity, which is the point source of the high noise generation (ref. 19).

Fan

Utilizing the previous design procedure, a small experiment was made of a 3D-printed fan as a replacement for a small box fan, such as those used in electronics cooling applications, or environmental air circulation and cooling in industrial applications. Minimal disruption of the fan unit being desirable, form factor fit, and reuse of the existing installation and fan housing were requirements. To this end, the new fan was designed using the same airfoils, the same chord lengths, and the same planforms as the original fan blade assemblies, as shown in figure 24 (left, center, and right). The only variance was to change the twist distribution of the blades, and 3D print a new fan blade assembly. There were five blades around the hub, and the new twist was calculated. The power settings for the fan unit were 23.5 VDC, the background ambient noise level was 75.8 dB, the motor alone (no fan blades installed) was 85.4 dB, the original fan blade assembly was 92.1 dB (7.6-mph flow velocity), and the new fan blade assembly was 86.2 dB (8.6-mph flow velocity). The result is a 24-percent increase in fan flow velocity with an 88-percent reduction in decibel noise level.

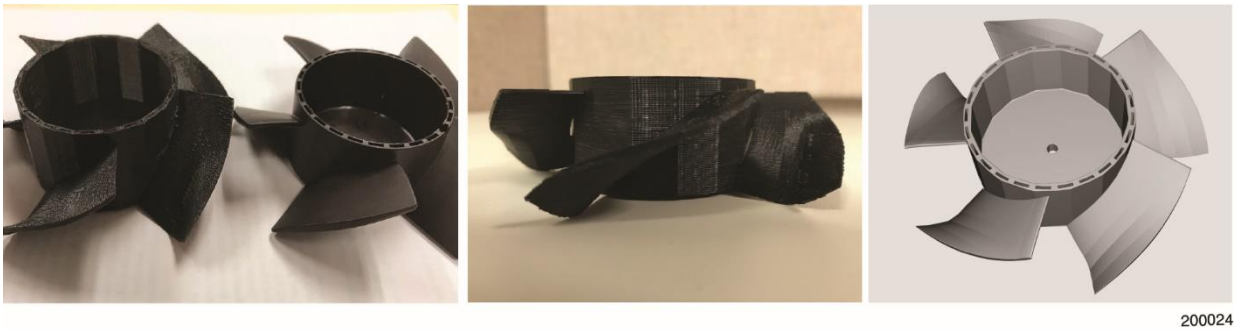

Figure 24. Fan assembly: (left) a new fan blade assembly; (center) the original fan assembly; and (right) new fan blade assembly 3D print graphic.

Wind Tunnel Test

A wind tunnel entry was made in the National Aeronautics and Space Administration (NASA) Langley Research Center (LaRC) (Hampton, Virginia) 12-ft low-speed wind tunnel (figure 25). The model was a Prandtl-D configuration of 6-ft span. The data collected from the wind tunnel affirmed many of the same things we had learned from our flight experiments. Sample data from the wind tunnel entry are shown in figure 26.

Figure 25. The Prandtl-D wind tunnel image.

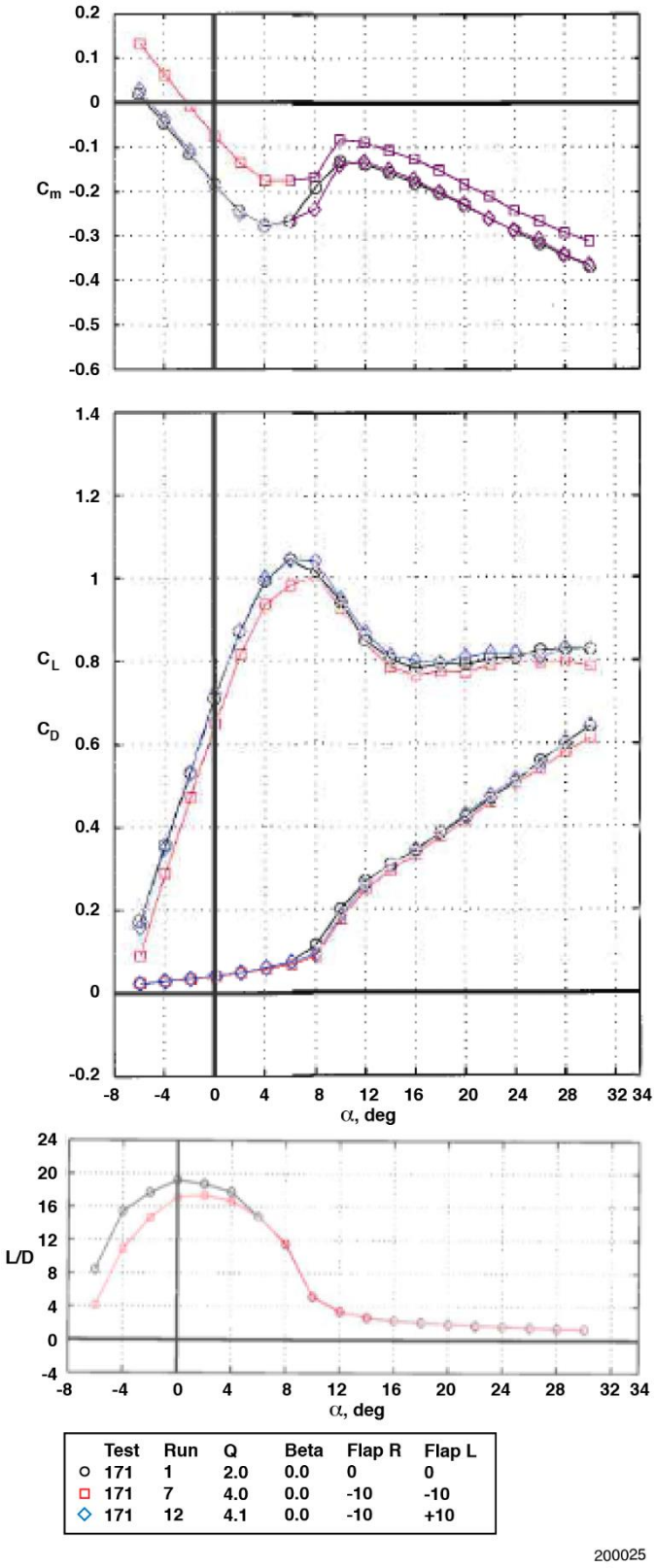

Figure 26. Wind tunnel data.

Conclusions

Aircraft using the Prandtl bell-shaped spanload have been flown and investigated. The results of this research have shown many previously held assumptions need to be reconsidered. Traditional approaches to the creation of aircraft using the Prandtl bell-shaped spanload have required considerable work to be rethought.

Part of the development of this work involved the use of inverse methods. The usual approach to the computational fluids problem is to create a geometry of the aircraft. Once the geometry exists, then the computational fluids solution can exist. The problem of creating the geometry remains. A very small segment of the computational fluid dynamics world has looked to inverse solutions. This thought process design approach begins with the idea of what the flow must look like in the end. Many simplifying assumptions must be made so that the mathematical solution to the inverse problem is tractable.

The beauty of this approach is that the endpoint is the beginning. The difficulty is in the selection of the simplifying assumptions so that they do not negate the validity of the final solution.

Much of the approach to aeronautics in recent years has concentrated on a forward method iterative approach. At the same time, it is known that there exists an inverse method to design wings. The inverse approach is very abstract and was only applicable to Horten spanloads. It was known that the Horten spanloads and the Prandtl bell-shaped spanload had different constraints and resulted in different spanloads. A more generic inverse tool was desired that would allow the design of wings, specifically Prandtl bell-shaped spanload wings. Such a tool has been developed; the tool allows variable taper (or variable chord length distribution), aspect ratio, sweep, airfoils, and design lift coefficients. The output of the tool is the twist distribution. The beauty of this tool is that the spanload is the initial condition for the wing design. The difficulty is that the simplifying assumptions (lifting line and thin airfoil) do not negate the final wing solution. This report is the validation of the Prandtl bell spanload and this inverse tool.

Appendix: Remaining Areas of Research

Many areas of research remain to be solved using the Prandtl bell-shaped spanload approach for flight, some examples are given below. This content is not exhaustive, the answers are not intuitively obvious, and current analytical approaches fail to encompass solutions to these problems.

Mean Aerodynamic Chord and Center of Gravity

The classical “mean aerodynamic chord” argument fails when using the Prandtl bell-shaped spanload. The classical approach makes assumptions about the effectiveness of each chord length of the geometry of the wing.

Mean aerodynamic chord (MAC) is a fundamental property used to characterize an aircraft wing. The MAC is defined as “the chord of an imaginary airfoil which would have force vectors throughout the flight range identical with those of the actual wing” (ref. 20). In other words, the wing can be characterized by resolving the entire lift distribution to a single force about the MAC. As such, both the length of the MAC and its y-coordinate are important determinations.

Historically, the MAC has often been calculated purely geometrically (ref. 21) by locating the centroid of the wing geometry in the XY plane using area moments in the y-axis and taking the chord measurement passing through that point, as shown in equation (A1):

$$\bar{y} = \frac{\sum_i A_i y_i}{\sum_i A_i} \tag{A1}$$

where the wing is subdivided into “panels,” the *i*th panel possessing an area A_i and a centroid with *y*-coordinate y_i. If the wing were to have a constant lift distribution all along its span, this calculation would be the exact solution. In practice, however, this is not the case. For the ubiquitous elliptical lift

distribution this approximation is a viable one, as has been seen experimentally; however, the method bears room for improvement. One method uses force moments essentially about the x-axis and finding the centroid of the lift distribution curve to account for the non-uniform spanload, as shown in equation (A2):

$$\bar{y} = \frac{\sum_i L_i y_i}{\sum_i L_i} \tag{A2}$$

where Li is the load borne by the ith panel. The lift distribution is now accounted for, but the geometry of the wing is neglected. An ideal solution would consider both factors: the influence of each panel would be weighted more if it were of longer chord and if it bore more dynamic flight load. The centroid of the area defined by a curve is essentially found by "weighting" different geometries based on some factor; consider now that this factor is defined to be the product of the local load and the area over which it is applied, equation (A3):

$$\bar{y} = \frac{\sum_i L_i A_i y_i}{\sum_i L_i A_i} \tag{A3}$$

or, if the lift and chord distributions are known as analytical continuous functions, equation (A4).

$$\bar{y} = \frac{\int L(y)c(y)ydy}{\int L(y)(y)dy} \tag{A4}$$

This proposed method incorporates both wing geometry and load distribution into the MAC calculation. The Prandtl bell-shaped spanload is designed to place the majority of the flight load near the centerline; the load tapers to zero at the wingtip.

As can be seen, this distribution is drastically different from a uniform spanload, implying that there will be even more error calculating the MAC using the geometry method than for the elliptical spanload. For purposes of analysis, consider the Prandtl-D3 airframe, a 25-ft wingspan research glider built with this spanload. The Prandtl-D3 wing also deviates from a perfect rectangle (as would be assumed if geometry were neglected in MAC calculation) tapering from a root chord of 30.8 in, down to only 8 in at the wingtip. Observing constant taper, the chord function can be written, as shown in equations (A5) and (A6):

$$c(y) = -0.15y + 30.5 \tag{A5}$$

$$L(y) = L_0\left(1 - \left(\frac{2y}{b}\right)^2\right)^{3/2} \tag{A6}$$

where *y* is measured in inches from the root. Using the two functions L(y) and c(y), the MAC can be calculated using each of the three methods listed above.

Indeed, the results vary significantly. Considering both geometry and load distribution skews the MAC location drastically inboard, which may be expected for the bell distribution, more work is required to confirm this phenomenon.

The proper MAC can now be determined experimentally. The aircraft was found to be balanced about a center of gravity placed at 12.8 percent of the geometric MAC, aft of the leading edge, along the (geometric) MAC line. By defining the MAC to be determined where the 0.128-geometric MAC line crosses the quarter chord line, a MAC value of 23.28 is determined, as shown in table A1.

Table A1. Mean aerodynamic chord calculated for the Prandtl-3 glider using each of the three described centroid methods.

Method	MAC	MAC location, in	MAC location, percent of half-span
Geometry	22.35	53.48	35.65
Lift distribution	21.5	60.0	40
Geometry and lift distribution	26.9	24.07	16
EXPERIMENTAL	23.28	48.15	32

Notice that the crude geometry and lift-distribution-weighted method proposed above provides a solution at almost exactly half as far outboard along the wing compared to the experimentally-determined solution. Further tests would need to be conducted on other aircraft with elliptical and bell-shaped distributions to examine whether this development is actually a trend or merely an incredible coincidence.

A MAC calculation method was developed that incorporated both wing geometry and lift distribution; this method would be particularly useful for wings exhibiting load distributions deviating significantly from a uniform spanload. This proposal is in a very early stage; as time passes it will be interesting to investigate this apparently striking link, perhaps showing how experimental results compare to this method.

Efficiency "Hump"

There appears to be an "efficiency hump" being created by wings that use the Prandtl bell-shaped spanload compared to the wings created by the elliptical spanloads of Prandtl. Designs that use the 1921 Prandtl spanload have a broad area of near-peak efficiency.

Based on the construct arguments used in the formulation of the MAC, changes in the angle of attack would be identical across the entire span, and the changes to the upwash and subsequently to the downwash would be identically commensurate. The end result would be that the wing would respond in a nearly 2D way to changes in the angle of attack over a broad range of angles of attack.

Moving forward to the Prandtl bell-shaped spanload, there now exists a 3D flow solution that is wedded to the geometry and upwash/downwash flow field. Changes to the wing angle of attack in this case will force the wing, its designed-in twist, and the flow-field solution, to be further off-design as the angle of attack moves away from the design point. The result would lead to a drop in the efficiency from the optimal point, implying that there would exist an "efficiency hump" for the bell-shaped spanload. In other words, the design is sensitive to off-design points.

In comparing the two spanloads, the elliptical spanload would be broad and the bell-shaped would be narrow. The elliptical spanload would appear as a broad region of relatively high efficiency for a rather broad range of angles of attack. The bell-shaped spanload would have higher efficiency than the elliptical but over a more limited range, appearing as a narrower, more rounded peak above the broad elliptical curve.

This condition would also be true of the propeller, fan, impeller, rotor, compressor, and turbine solutions. That is, the Betz 1921 solution would appear to be a broad curve, and the bell-derived solution would be a narrow-rounded peak above the 1921 Betz curve.

Indeed, this condition has been observed (though in an uncontrolled manner). A classical propeller was tested on a small electric unmanned aircraft system (UAS). Static thrust was measured, and, using a radar gun, the top speed was observed. Later, the same aircraft was fitted with a bell-derived solution propeller. The static thrust was observed to be less (approximately 12 percent), and the top speed was also observed to be slightly reduced (approximately four percent). The midrange acceleration, however, was

noticeably improved. The pilots reported the propeller had much more “snap” in the midrange during aerobatic maneuvers. Unfortunately, before the classical propeller could be tested again, there was damage to the propeller and subsequent testing was not completed.

Thought experiments have been conducted to improve the range of applicability of the derived bell solution. For wings, the answer would be to apply a flap across the span of the wing. With suitable deflections, the band of peak efficiency could be moved around. At the present time (sans analysis) a twisted flap appears to be the most desirable option in order to accommodate the twisted flow field development at off-design conditions. The exact nature of this twisted flap deflection remains unknown. Such a design development for the propeller, rotor, fan, compressor, impeller, and turbine, would be challenging.

Variations in the Spanload of Soaring Birds

Another question arises with respect to variations in the spanload between soaring birds. The two archetypes of soaring birds are the albatross (pointed wingtip without slots) and the condor (spread wingtip with slots). The albatross type clearly behaves in a manner expected of the fully developed Prandtl bell-shaped spanload: typically, the feathers are pointed and do not exhibit an upward deflection, indicating the load tapers to zero at the wingtip. In the condor type, typically the feathers are spread apart with slots between them at the tips, and the feathers exhibit a gentle upward deflection as though the tips are carrying a small load.

In the Prandtl bell paper (ref. 22), a variable μ is introduced. By varying μ from zero to one, the spanload varies from elliptical (μ=0) to the fully developed Prandtl bell (μ=1). Based on the limited data (ref. 23) and photographs of pelicans, an estimate can be made of the downwash-upwash-crossover-point (DUCP) for these birds. Note that the data on the kestrel (see ref. 23) possibly includes Reynolds Number effects due to the small size in comparison to the larger birds such as the pelican. Soaring land birds (archetype condor) that use a loiter flight strategy reduce their μ value slightly. Soaring sea birds (archetype albatross) that use a range strategy increase their μ value.

Inferring that DUCP represents the vortex location, estimates of μ appear to be in the range of 0.75 to 1.0, as shown in figure A1.

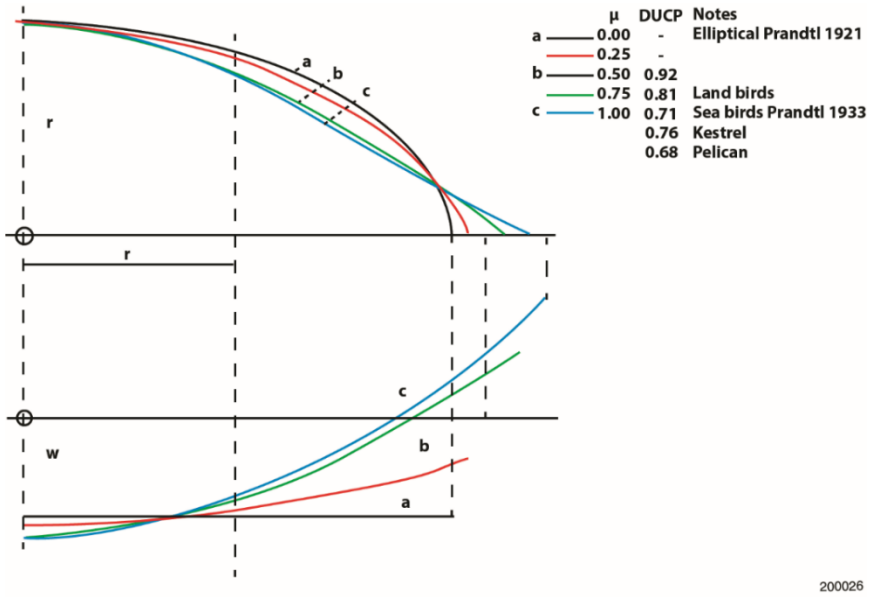

Figure A1. Variations in Prandtl bell μ from zero to one gives rise to the spanload variations and the effect on downwash. Of note, are the downwash-upwash-crossover-point effects and how these correspond to the two archetype soaring models (condor versus albatross).

Albatross Dynamic Soaring

Much recent literature has been written about the soaring flight of the albatross (ref. 24), although more work remains to be done in this research. No validated wind-field boundary layer has been measured against which to compare against the models. Furthermore, no validated flight mechanics data have been gathered for this work to date. The ability to use a small UAS to produce dynamic soaring in the boundary layer over the surface of the Earth would be an impressive accomplishment. In order for the small UAS to be similar to the albatross, the aircraft would need to be designed without a vertical tail. As a result, the bell-shaped spanload would be preferred because it would improve the handling of such a vehicle.

Other extensions of this work remain. Other obstacles would create wind shear in the boundary layer over the surface of the Earth. For instance, a sailing ship, while tacking downwind, would create a stronger shear on one side of its wake than the other, simply because of its cross-field movement through the wind field. In this case, the birds would find it more advantageous to soar on one side of the wake and not the other. Additionally, the birds might find the ship useful in reducing the workload needed to soar by selecting the easier side on which to soar in the wake shear. Perhaps it is not just the attraction of food behind the ship that is of interest, but the energy assist to remaining aloft in soaring flight.

Turbine

Some mention has been made of the application of the approach to the optimization of propellers. By extension, the same approach can be used for rotors, fans, and compressor blades. It should also be possible to do the same for impellers in centrifugal pumps. Turbines, however, remain a unique problem.

Propellers, rotors, fans, compressors, and impellers are powered and are imparting energy to the working fluid. This state is referred to generically as the propeller problem. Turbines are the opposite: turbines extract energy from a working fluid. The turbine optimization problem is the opposite of that of the propeller problem. The propeller problem optimization is +1; the turbine problem optimization is -1.

The design of a turbine created in this way has not been accomplished. This work remains to be completed.

Transonic/Supersonic

The challenge of transonic applications remains for wings and propulsion systems made with these solutions; however, given that the necessary requirement of such a solution is upwash, it may be possible to extend the approach to supersonic speeds. The leading edge would necessarily be required to be subsonic to achieve the needed upwash flow field. Thus, for any given supersonic Mach number, a corresponding swept wing with a subsonic leading edge could be designed and to which the appropriate twist to achieve a Prandtl bell-shaped spanload could be created.

References

1. Prandtl, L., *Theory of Lifting Surfaces. Part 1,* NACA-TN-9, 1918.

2. Prandtl, L., *Theory of Lifting Surfaces. Part 2,* NACA-TN-10-Pt-2, 1919.

3. Prandtl, L., *Applications of Modern Hydrodynamics to Aeronautics. [In Two Parts]*, NACA-TR-116, 1921.

4. Munk, Max M., *The Minimum Induced Drag of Aerofoils*, NACA-TR-121, 1921.

5. Prandtl, L., *Theory of Lifting Surfaces. Part 1*, NACA-TN-9, July 1920.

6. Horten, Reimar, personal notes, 1950, (unpublished).

7. Horten, Reimar, "Lift Distribution on Flying Wing Aircraft," *Soaring,* pp. 40-42, June, 1981.

8. Horten, Reimar, and Peter F. Selinger (translator), *"Nurflügel: die Geschichte der Horten-Flugzeuge 1933-1960,"* (German edition), Weishaupt, 1983.

9. Bowers, Albion H., Oscar J. Murillo, Robert "Red" Jensen, Brian Eslinger, and Christian Gelzer, *On Wings of the Minimum Induced Drag: Spanload Implications for Aircraft and Birds,* NASA/TP-2016-219072, March 2016.

10. Jones, Robert T., *The Spanwise Distribution of Lift for Minimum Induced Drag of Wings Having a Given Lift and a Given Bending Moment*, NACA-TN-2249, Dec. 1950.

11. Klein, Armin, and Sathy P. Viswanathan, "Approximate Solution for Minimum Induced Drag of Wings with Given Structural Weight," *Journal of Aircraft,* Vol. 12, No. 2, pp. 124-126, Feb. 1975.

12. Jones, R.T., "Minimizing Induced Drag," *Soaring*, pp. 26-29, Oct 1979.

13. Wakayama, Sean, and Ilan Kroo, "Subsonic Wing Planform Design Using Multidisciplinary Optimization," *Journal of Aircraft,* Vol. 32, No. 4, pp. 746-753, July-Aug 1995.

14. Breguet, M. Louis, "L'AVIATION D'HEIR & DE DEMAIN," *L'Aerophile,* pp. 265-272, Sept. 15, 1921.

15. Kuchemann, D., "Die Aerodynamische Entwicklung von Schlanken Flugeln fur den Uberschallflug," DK 533.693.3.011.5, 1961.

16. Maine, Richard E., and Kenneth W. Iliff, *Application of Parameter Estimation to Aircraft Stability and Control: The Output-Error Approach,* NASA-RP-1168, June 1986.

17. Margason, Richard J., and John E. Lamar, *Vortex-Lattice FORTRAN Program for Estimating Subsonic Aerodynamic Characteristics of Complex Planforms*, NASA-TN-D-6142, February 1971.

18. Pena, Francisco, Benjamin L. Martins, and W. Lance Richards, *Active In-flight Load Redistribution Utilizing Fiber-Optic Shape Sensing and Multiple Control Surfaces*, NASA/TM-2018-219741, February 2018.

19. Marte, Jack E., and Donald W. Kurtz, *A Review of Aerodynamic Noise From Propellers, Rotors, and Lift Fans*, NASA-CR-107568, January 1970.

20. National Advisory Committee for Aeronautics, *Nomenclature for Aeronautics,* NACA-TR-474, January 1939.

21. Diehl, Walter S., *The Mean Aerodynamic Chord and The Aerodynamic Center of a Tapered Wing*, NACA-TR-751, January 1942.

22. Prandtl, Von L., "Über tragflügel kleinsten induzierten widerstandes," *Zeitschrift für Flugtechnik und Motorluftschiffahrt*, München, Deustchland, 1 VI, 1933.

23. Spedding, G. R., “The Wake of A Kestrel (Falco Tinnunculus) in Gliding Flight,” *Journal of Experimental Biology* 127, pp. 45- 57, 1987.

24. Sachs, Gottfried, et al., “Flying at No Mechanical Energy Cost: Disclosing the Secret of Wandering Albatrosses,” *PLOS ONE,* Vol. 7, No. 9, Sept. 2012.